Energy & Environmental Science

ROYAL SOCIETY OF CHEMISTRY

PAPER

View Article Online
View Journal | View Issue

Published on 29 2021. Downloaded by Fail Open on 23.07.2025 09:12:30.

Check for updates

Cite this: *Energy Environ. Sci.*, 2021, **14**, 3510

A flame-retardant polymer electrolyte for high performance lithium metal batteries with an expanded operation temperature†

Jingwei Xiang,‡[a] Yi Zhang,‡[a] Bao Zhang,[b] Lixia Yuan,*[a] Xueting Liu,[a] Zexiao Cheng,[a] Yan Yang,[a] Xinxin Zhang,[a] Zhen Li,[a] Yue Shen,[a] Jianjun Jiang[b] and Yunhui Huang*[a]

Polymer electrolytes with high ionic conductivity, good interfacial stability and safety are in urgent demand for practical rechargeable lithium metal batteries (LMBs). Herein we propose a novel flame-retardant polymerized 1,3-dioxolane electrolyte (PDE), which is *in situ* formed *via* a multifunctional tris(pentafluorophenyl)borane (TB) additive. The *in situ* formed PDE not only affords an integrated battery structure with stabilized electrode–electrolyte interface, but also achieves good flame retardancy, significantly expanded operating temperature limit and improved oxidative stability. Moreover, TB also contributes to a highly stable LiF-rich solid electrolyte interphase (SEI). In addition, the PDE has good compatibility with electrodes and polypropylene (PP) separator, hardly increasing the thickness of the battery, and the amount of additive TB is small, so there is no loss of gravimetric or volumetric energy density due to the polymerization. Based on the *in situ* formed PDE, Li–S batteries without the addition of $LiNO_3$ demonstrate excellent cycle stability (>500 cycles) and a wide operating temperature (−20 to 50 °C); the high voltage Li–$LiNi_{0.6}Co_{0.2}Mn_{0.2}O_2$ and Li–$LiFePO_4$ batteries both exhibit excellent electrochemical performance (>1200 cycles). In addition, the ultrasonic imaging technique developed by our group also demonstrates no gas generation inside pouch cells using PDE. This work provides a facile and practical approach to design a highly stable polymer electrolyte for high performance LMBs.

Received 6th January 2021,
Accepted 29th April 2021

DOI: 10.1039/d1ee00049g

rsc.li/ees

Broader context

Due to the limited energy density of traditional lithium-ion batteries, it has been difficult to meet the growing energy demand in emerging fields. Lithium (Li) metal anode has drawn tremendous attention due to its highest theoretical specific capacity (3860 mA h g^{-1}) and the lowest redox potential (−3.04 V *vs.* standard hydrogen potential). Unfortunately, the uncontrolled growth of Li dendrites and the low Coulombic efficiency hinder the commercialization of Li metal anodes. Compared with liquid organic electrolytes, polymer electrolytes are considered to be ideal in combination with Li metal anodes due to their good plasticity and good adhesion to electrodes. However, the flame-retardant properties of the polymer electrolyte and the interfacial stability between electrolyte and electrode still need further improvement. In this work, we develop a new strategy to prepare an *in situ* polymerized 1,3-dioxolane electrolyte (PDE) *via* a multifunctional tris(pentafluorophenyl) borane (TB) additive. The *in situ* formed PDE not only affords an integrated battery structure with stabilized electrode–electrolyte interface, but also achieves good flame retardancy, significantly expanded operating temperature limit and improved oxidative stability. Based on the *in situ* formed PDE, the Li–sulfur, high voltage Li–$LiNi_{0.6}Co_{0.2}Mn_{0.2}O_2$ and Li–$LiFePO_4$ batteries all exhibit excellent electrochemical performance.

Introduction

Lightweight and rechargeable lithium-ion batteries are now widely applied from mobile phones to electric cars. They are also considered as one of the most promising candidates as a bridge between the electric energy from renewable solar/wind power and the electric grid, making a fossil fuel-free society possible.[1–3] However, due to the limited energy density of the electrode materials based on the insertion mechanism, traditional lithium-ion batteries have struggled to meet the growing energy needs of the emerging areas. Therefore, it is of vital

---

[a] *State Key Laboratory of Material Processing and Die & Mold Technology, School of Materials Science and Engineering, Huazhong University of Science and Technology, Wuhan, Hubei 430074, China. E-mail: huangyh@mail.hust.edu.cn, yuanlixia@hust.edu.cn*

[b] *School of Optical and Electronic Information, Huazhong University of Science and Technology, Wuhan, Hubei 430074, China*

† Electronic supplementary information (ESI) available. See DOI: 10.1039/d1ee00049g

‡ These authors contributed equally to this work.

This journal is © The Royal Society of Chemistry 2021

Published on 29 2021. Downloaded by Fail Open on 23.07.2025 09:12:30.

importance to develop advanced electrode materials with higher energy densities.[4,5] Among all the potential solid candidates, lithium (Li) metal anode has drawn tremendous attention due to its highest theoretical specific capacity (3860 mA h g^{-1}) and the lowest redox potential (−3.04 V *vs.* standard hydrogen potential).[6–8] However, the practical application of the rechargeable Li anode based on the traditional liquid organic electrolyte faces a seemingly impassable obstacle: the inhomogeneous deposition of lithium ions in liquid organic electrolytes results in uncontrollable dendritic growth, which leads to reduced Coulombic efficiency (CE), significantly shortened cycle life and even short-circuiting. In addition, the thermodynamically unstable and flammable liquid organic electrolytes further increase the safety risks of the lithium metal batteries (LMBs).[9,10]

Compared with liquid organic electrolytes, solid-state electrolytes (SSEs) have attracted tremendous attention in recent years because of their inherent non-leakage and high safety. So far, the solid-state lithium battery has become a research hotpot in both academic and industrial world.[11–13] Organic polymer SSEs (so-called solid-state polymer electrolytes (SPEs)) are one of the most important SSEs[14–16] due to its good plasticity, good adhesion to electrodes, low cost and manufacturing scalability.[17–19] It is considered as an ideal choice to pair with Li metal anode. However, there are still several challenges to overcome in the practical application of SPEs[20,21] (Fig. 1a). The room-temperature ionic conductivity of the SPE is typically 2–3 orders of magnitude lower than that of the liquid electrolyte,[22] so that the reported polymer batteries always work at ∼60 °C. Due to the limited mechanical strength of the polymer electrolyte and the traditional tape casting preparation route, the thickness of SPE is in the range of 50–1000 μm, which is much thicker than the separator (10–30 μm) in the liquid battery.[23] The thick film not only decreases the energy density of the battery but also increases the transfer distance of Li-ions which places stringent requirements on the conductivity of the electrolyte. Although the plasticity of SPE makes the building of the electrode/electrolyte interface is relatively easier than the inorganic solid electrolyte system, the traditional roll by roll route for the battery assembling cannot guarantee the integrated contact of the different parts of the battery so that the internal resistance is much higher than that of the batteries with liquid electrolytes. In addition, the most reported SPEs based on poly(ethylene oxide) (PEO) are still

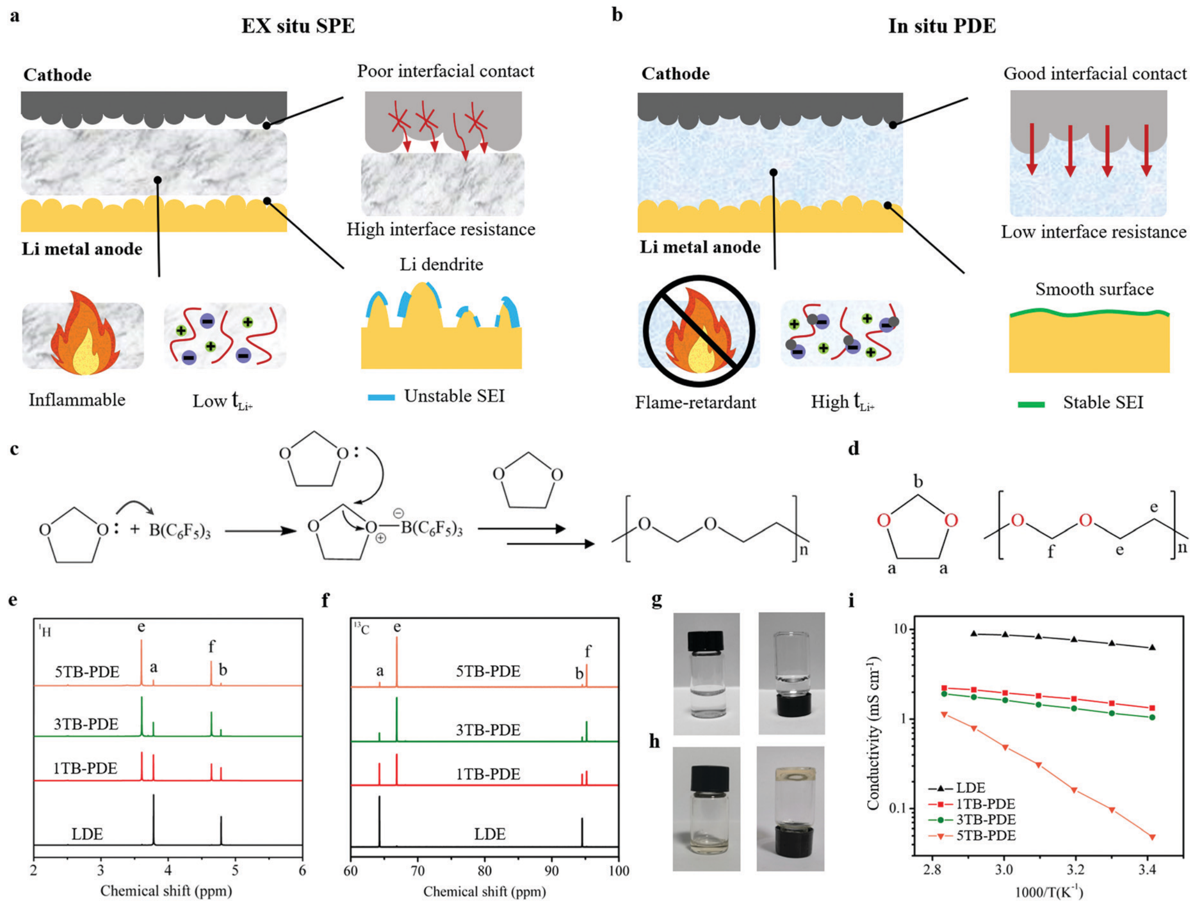

Fig. 1 Mechanism and characterization of PDE. (a) Schematic diagram of *ex situ* SPE with low ionic conductivity, unstable SEI, poor interfacial stability and inflammable. (b) Schematic diagram of PDE with high ionic conductivity, stable SEI, good interfacial stability and flame-retardant. (c) Schematic diagram of the polymerization mechanism of PDE. (d) Structure formulas of DOL and poly-DOL. (e and f) Hydrogen (e) and carbon (f) NMR spectra of LDE, 1TB-PDE, 3TB-PDE, 5TB-PDE, respectively. (g and h) Digital photographs of LDE (g) and 3TB-PDE (h). (i) Temperature-dependent ionic conductivity of LDE, 1TB-PDE, 3TB-PDE, 5TB-PDE, respectively.

Published on 29 2021. Downloaded by Fail Open on 23.07.2025 09:12:30.

flammable, leading to poor safety. All these problems plague the market penetration of the polymer batteries.

In recent years, the mechanical properties and ionic conductivities of SPEs are greatly improved *via* polymer skeleton modification[24–26] and/or adding inorganic fillers.[27–30] But the interfacial transport keeps as one of the bottlenecks of the polymer system throughout.[31] The novel *in situ* polymerization route has a unique advantage in building fast interfacial transport. It has been originally used to prepare gel polymer electrolytes:[32–34] a certain amount of polymer monomer is directly added into the liquid electrolyte; the gel polymer electrolyte or gel polymer batteries are formed *via* initiating the polymerization of the monomer molecules in the liquid electrolyte. Because the precursor electrolyte has a similar viscosity as the traditional liquid electrolyte, it can easily penetrate into the entire region of the cell and the following polymerization will result in an integrated three-dimensional network throughout the whole battery. The integrated structure guarantees the compact contact between the solid electrolyte and the electro-active particles. As a result, the interfacial resistance of the battery using *in situ* formed polymer electrolyte is significantly decreased than that of the cell using the pre-manufactured polymer film as the electrolyte.[35–37] More recently, several commonly used solvents in LIBs, like 1,3-dioxolane (DOL),[38,39] fluoroethylene carbonate (FEC),[40] 1,3,5-trioxane (TXE)[41] and tetrahydrofuran (THF),[42] which can undergo polymerization reaction under initiation of the initiator, have been used to form a polymer electrolyte *via in situ* polymerization. Here no extra monomers are needed and the resulted solid electrolyte can be controlled between a dry polymer and a gel polymer *via* controlling the polymerization degree. DOL is widely used as solvent or co-solvent for the liquid electrolyte of lithium–sulfur (Li–S) battery and it can form a polymer matrix for the polymer electrolyte *via* ring-opening polymerization. Several previous works have demonstrated that the *in situ* formed poly-DOL electrolyte can well serve in Li–S and Li–$LiFePO_4$ batteries, both of which show significantly improved interfacial transport.[38,39,43]

In this work, we develop a new strategy to prepare an *in situ* polymerized DOL electrolyte (PDE) of flame retardation and largely expanded operation temperature range *via* a multifunctional tris(pentafluorophenyl) borane (TB) additive. The *in situ* polymerization route guarantees the integrated structure of the cell in which the polymer electrolyte spreads over the entire region of the battery to afford a stabilized electrochemical reaction interface in both anode and cathode. Here TB is introduced not only as an initiator but also as a multifunctional additive. In addition to triggering the cationic polymerization of DOL, a small amount of TB also works as a high-efficient flame retardant *via* generating fluorine radicals, realizing a non-flammable polymer electrolyte (Fig. 1b). Furthermore, the TB with high fluoride content contributes to the formation of a highly stable LiF-rich SEI and improves the Li-ion transference number from 0.19 to 0.58 by immobilizing the anions. In addition, the *in situ* formed PDE has good compatibility with electrodes and the polypropylene (PP) separator, hardly increasing the thickness of the battery, and the amount of additive TB is small, so there is no loss of gravimetric or volumetric energy density due to the polymerization. When PDE is applied to Li–S battery, it demonstrates an ultraslow capacity decay rate of 0.094% throughout 550 cycles and the operation temperature range of the battery is expanded to −20–50 °C. Furthermore, the polymer battery shows excellent flexibility and high resistance to mechanical abuse: after being bent and folded or even cut in the air, the Li–S polymer pouch cell can still be able to power the light-emitting diode (LED) lamp. Benefited from the improved oxidation stability, the novel PDE can also well serve the high voltage battery systems like Li|$LiFePO_4$ and Li|$LiNi_{0.6}Co_{0.2}Mn_{0.2}O_2$ (NCM_{622}). Moreover, it is noted that the *in situ* formed PDE is conformal with the electrodes and the polypropylene (PP) separator, which adds almost no thickness to the battery, so the use of PDE in batteries does not result in any loss of gravimetric or volumetric energy density. Subsequently, ultrasonic transmission mappings, which is an effective non-destructive technique developed by our group to investigate the state of the electrolyte inside a pouch cell, show no gas generation in the Li|PDE|$LiFePO_4$ pouch cell during cycles, further demonstrating the stability of PDE. This work provides a facile and practical approach to design a highly stable and safe polymer electrolyte for high performance rechargeable LMBs.

Results and discussion

Structure, kinetics and thermal stability of PDE

The essential chemical process of the cationic-induced ring-opening polymerization of DOL is summarized in Fig. 1c. The boron atom in TB, a Lewis acid, first attaches to the oxygen atom of DOL, and then the ring-open polymerization is initiated. The liquid DOL electrolytes (LDEs), DOL + 2M lithium bis(trifluoromethanesulfonyl)imide (LiTFSI), with 1, 3 and 5 wt% TB additives are named as 1TB-PDE, 3TB-PDE, 5TB-PDE, respectively. TB is dissolved into the LDE under stirring. The precursor electrolytes with TB additive spontaneously converted to PDE after resting at room temperature. The optical photographs in Fig. 1g and h and Fig. S1 (ESI†) demonstrate the transformation of LDE from a well-flowing liquid to a solid electrolyte with 1 wt%, 3 wt% and 5 wt% TB addition, respectively. Nuclear magnetic resonance (NMR) was used to identify the structures of PDEs. As shown in Fig. 1d and e, new ^1H and ^{13}C NMR peaks are observed with the polymerization of DOL. The new ^1H NMR peaks at 3.61 and 4.64 ppm are assigned to H on groups $–O–CH_2–CH_2–$ and $–O–CH_2–O–$, respectively, which are consistent with the repeated $–CH_2–O–CH_2–CH_2–O–$ unit of poly-DOL.[38] The ^{13}C NMR spectra are in accordance with the ^1H NMR spectra, further confirming the polymer structure (Fig. 1f). Meanwhile, when the TB concentration increases from 1 to 3 and 5 wt%, the fraction of the poly-DOL can be identified from the integrated area of the ^1H NMR spectra as 64%, 89% and 96%, respectively. The ionic conductivities of PDEs with different TB concentrations at a temperature range from 20–80 °C are shown in Fig. 1i. The ionic conductivity of 5TB-PDE at 30 °C is only 0.098 mS cm^{-1}, which is two orders of magnitude lower than that of LDE (6.91 mS cm^{-1}). In contrast, 1TB-PDE and 3TB-PDE demonstrate much higher ionic conductivities of 1.502 and 1.163 mS cm^{-1} at 30 °C, respectively,

This journal is © The Royal Society of Chemistry 2021

Published on 29 2021. Downloaded by Fail Open on 23.07.2025 09:12:30.

which are sufficient to meet the need of practical batteries. In the meanwhile, considering that 1TB-PDE is still in the quasi-liquid state due to the low polymerization degree (Fig. S1a, ESI†), 3TB-PDE is chosen as the optimal candidate. In the following discussion, the optimized electrolyte, 3TB-PDE, is abbreviated as PDE and its safety and electrochemical properties are systematically studied.

According to the ionic conductivity change of PDE in Fig. S2 (ESI†), it can be estimated that it takes ∼4 h for the phase conversion process, which guarantees the fully wetting of the electrode when assembling the battery. Fig. 2a shows the scanning electron microscope (SEM) image of the celegard 2400 separator. The original polypropylene (PP) film has a large number of pores and the thickness is ∼25 μm (Fig. 2b). For the separator with PDE infiltration, the original pores of the PP film are all blocked (Fig. 2d) and the thickness of the separator slightly increases to ∼27 μm (Fig. 2e). The flammability tests are shown in Fig. 2c: the LDE drenched separator burst into flame as soon as contacting with the fire. It took less than a second for the separator to burn out. In addition, the separator with PEO electrolyte filled also burst into flame when came in contact with the fire (Fig. S3, ESI†). In sharp contrast, the separator with PDE infiltration did not burn even when remained in contact with the flame for several seconds (Fig. 2f). The good flame retardancy comes from the fluorine free radicals generated by the thermal decomposition of TB which can effectively trap the highly reactive radicals of $H^\bullet$ and $OH^\bullet$, thus effectively preventing the separator burning.

Structure-dependent ion transport properties

In addition to the flame retardancy effect, TB also influences the solvent structure of the electrolyte. Due to the Lewis acid–base interaction, the B centre in TB interacts with the $TFSI^-$ anion group to form a large coordinate anion with low mobility, thus releasing more free Li ions and resulting in a high Li-ion transference number. The anion trapping effect of TB in PDE can be identified by Fourier-transform infrared spectroscopy (FTIR) and Raman spectroscopy. Fig. 3a and b show the detailed FTIR spectra of LDE and PDE in the range of 1165–1225 and 1280–1400 cm^{-1}. Obviously, the peaks of -CF_3 stretching of $TFSI^-$ shifts from 1198 cm^{-1} in LDE to 1193 cm^{-1} for PDE (Fig. 3a) and the peaks located at 1318.5 cm^{-1} for –SO_2 stretching in $TFSI^-$ shifts to 1320.5 cm^{-1} (Fig. 3b). Additionally, the peak of C–B shifts from 975 cm^{-1} in TB to 990 cm^{-1} in PDE (Fig. S4, ESI†). These peak shifts suggest the interaction between TB and $TFSI^-$ anions.[29,44–46] The Raman analysis also supports the conclusion. As shown in Fig. 3c, the peaks at 745.6 and 754.5 cm^{-1} correspond to the dissociated ions (D-ions) and ion-pairs (P-ions), respectively, which represents the intensity of the interaction between Li^+ and $TFSI^-$.[47–49] Obviously, PDE has a higher ratio of D-ions than that of LDE, indicative of more free Li ions in the polymer system. Afterwards, the Li-ion transference numbers of LDE and PDE were measured by chronoamperometry using Li/electrolyte/Li symmetric cells. The chronoamperometry curves and the AC impedances before and after polarization of the cells are shown in Fig. S5 and S6 (ESI†). There is a significant increase in Li-ion transference number from 0.194 of LDE to 0.584 of PDE, which is consistent with the FT-IR and Raman results (Fig. 3d) and the ionic conductivity of PDE at room temperature is 1.121 mS cm^{-1}, thus satisfying the needs of batteries (Fig. S7, ESI†). For better understanding the molecule structure and the ion dynamics, Molecular Dynamics (MD) simulations were performed to investigate the solvation structure of the electrolytes with and without TB additive. Fig. 3e-h show the snapshots of the simulated electrolytes. According to the calculated radial distribution functions ($g(r)$, solid lines) and coordination numbers ($n(r)$, dash lines) in Fig. 3i and j, the dominated peaks of

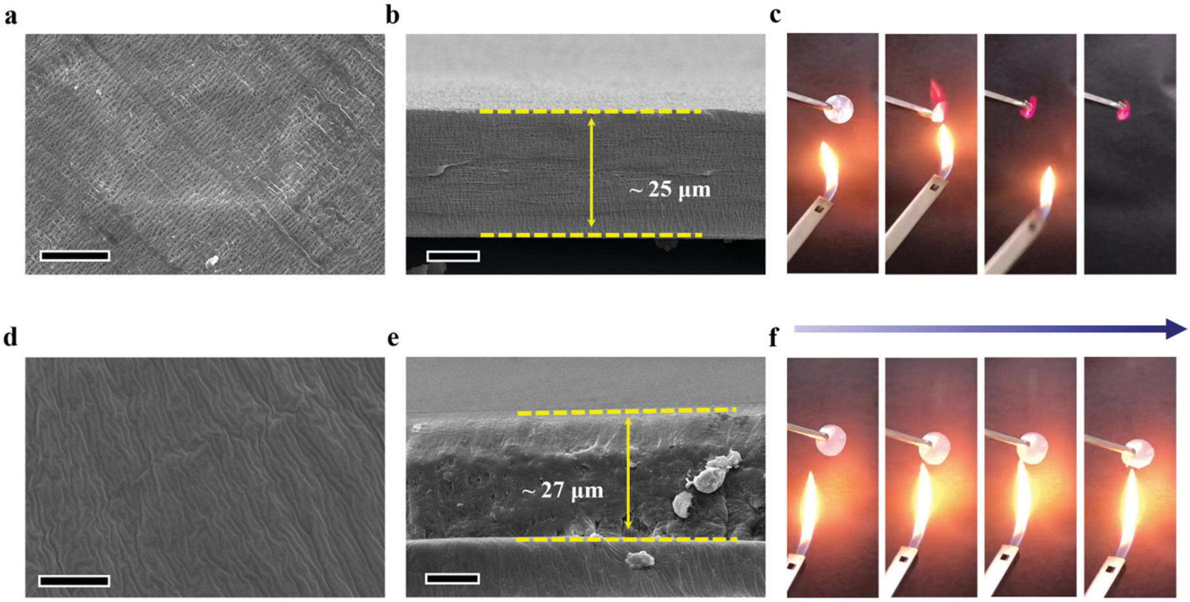

Fig. 2 Materials characterization and flame test. (a and b) Top-view (a) and cross-section (b) SEM images of the PP separator. (c) Flame test of the separator with LDE infiltration. (d and e) Top-view (d) and cross-section (e) SEM images of the separator after PDE infiltration. (f) Flame test of the separator with PDE infiltration. Scale bars, 10 μm (a, b, d and e).

Published on 29 2021. Downloaded by Fail Open on 23.07.2025 09:12:30.

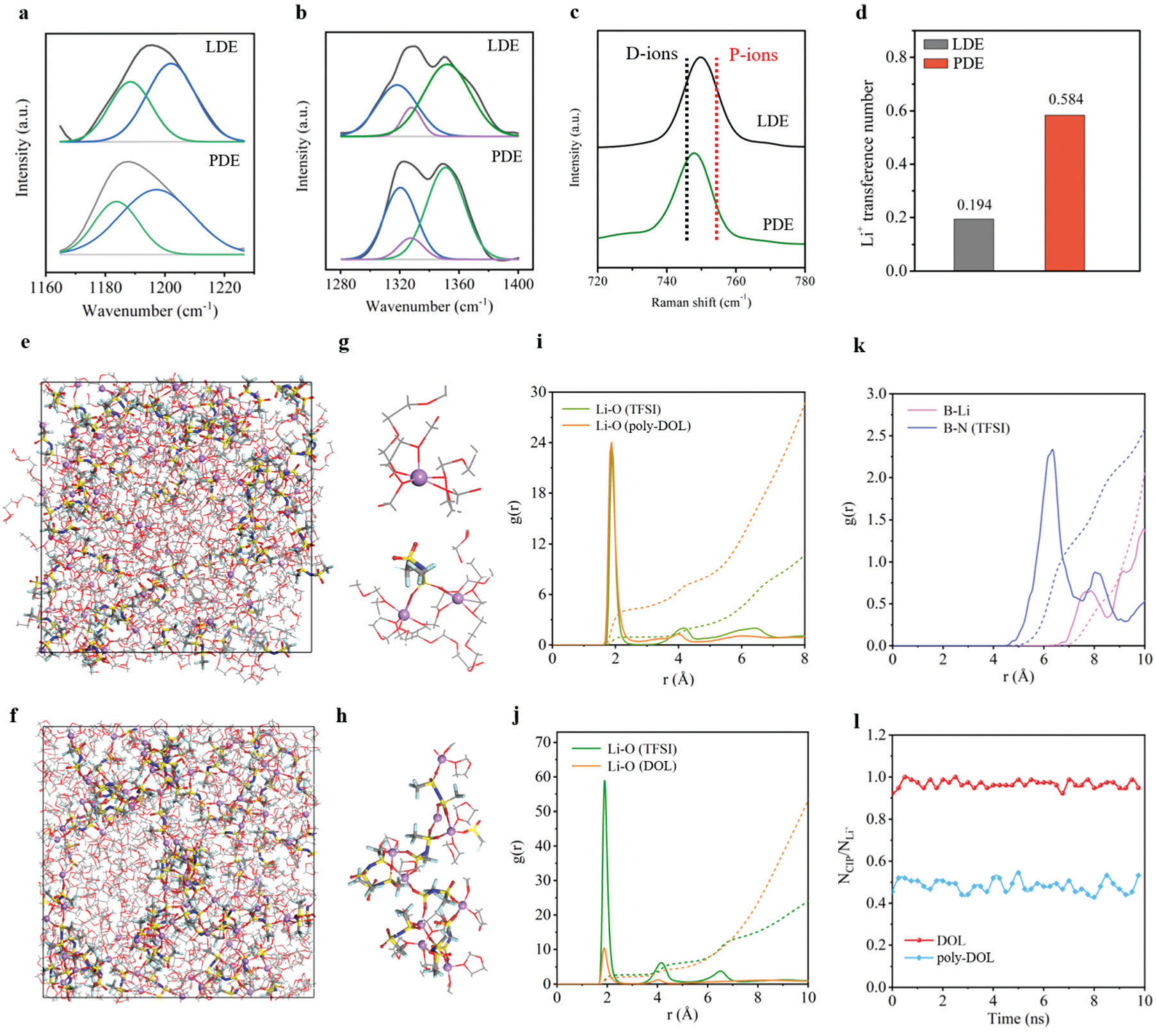

Fig. 3 Chemistry analysis and theoretical calculation of PDE. (a–c) FTIR (a and b) and Raman spectra (c) of LDE and PDE. (d) The Li^+ transference numbers of LDE and PDE. (e and f) Snapshots of PDE (e) and LDE (f) obtained by MD simulation at 25 °C. The Li^+ and their first coordinated shells are presented by ball and stick model, while the wireframes stand for free solvents. (g and h) Li^+ coordination structures of PDE (g) and LDE (h) electrolytes. Balls with various colors represent different atoms; Color code: red, O; blue, N; yellow, S; magenta, Li; brown, C; white, H. (i–k) Calculated radial distribution functions (*g*(*r*), solid lines) and coordination numbers (*n*(*r*), dash lines) for PDE (i and k) and LDE (j). (l) Contact ion pairs fraction of different solvents.

g(*r*) appear at 1.9 Å for Li–O ($TFSI^-$) and Li–O (poly-DOL) in PDE, indicating majority of Li^+ ions contact with both $TFSI^-$ anions and poly-DOL skeleton. In the LDE (Fig. 3j), the dominated peaks of *g*(*r*) appear at 1.9 Å for Li–O ($TFSI^-$), indicating majority of Li^+ ions and $TFSI^-$ anions are in direct contact. As shown in Fig. 3l, the fraction of contact ion pairs in PDE is significantly lower than that of LDE. The MD simulation results further confirms that the addition of TB is beneficial to weaken the interaction between $TFSI^-$ and Li^+, thus facilitating the dissociation of LiTFSI to release more Li^+. The enhanced Li-ion transference number of PDE can contribute to the improvement of the transmission capability of Li-ion in the electrolyte and facilitates the operation of the battery under special conditions, such as working at low-temperatures.

Interfacial stability and electrochemical performances

Li|Li symmetrical cells were assembled with PDE and LDE to investigate the compatibility with Li metal anode. After 50 cycles at 1 mA cm^{-2} for 2 mA h cm^{-2}, the surface of the Li metal anode harvested from the LDE is covered with Li dendrites, resulting in the deterioration of the interface stability (Fig. 4a). According to the cross-section SEM image (Fig. 4b), the thickness of the loose and porous reaction layer of the Li metal reached up to ~45 μm. When PDE is employed, the growth of Li dendrite is effectively suppressed and the Li metal anode demonstrates a much smoother surface (Fig. 4c). Fig. 4d shows that the thickness of the reaction layer is only ~12 μm. X-ray photoelectron spectroscopy (XPS) analysis further investigates the chemical state of the SEI on the Li metal anode in different electrolytes. For the SEI in LDE, as shown in Fig. 4e, the peak at 289.9 eV in the C1s spectrum belongs to CO_3^{2-} and COOR, which come from the decomposition of DOL.[38,50] Meanwhile, only weak signal of LiF can be detected in the F1s XPS spectrum (Fig. 4f). In comparison, for the SEI in PDE, the main peaks of C1s spectrum come from the polymer chain (Fig. 4h).

Published on 29 2021. Downloaded by Fail Open on 23.07.2025 09:12:30.

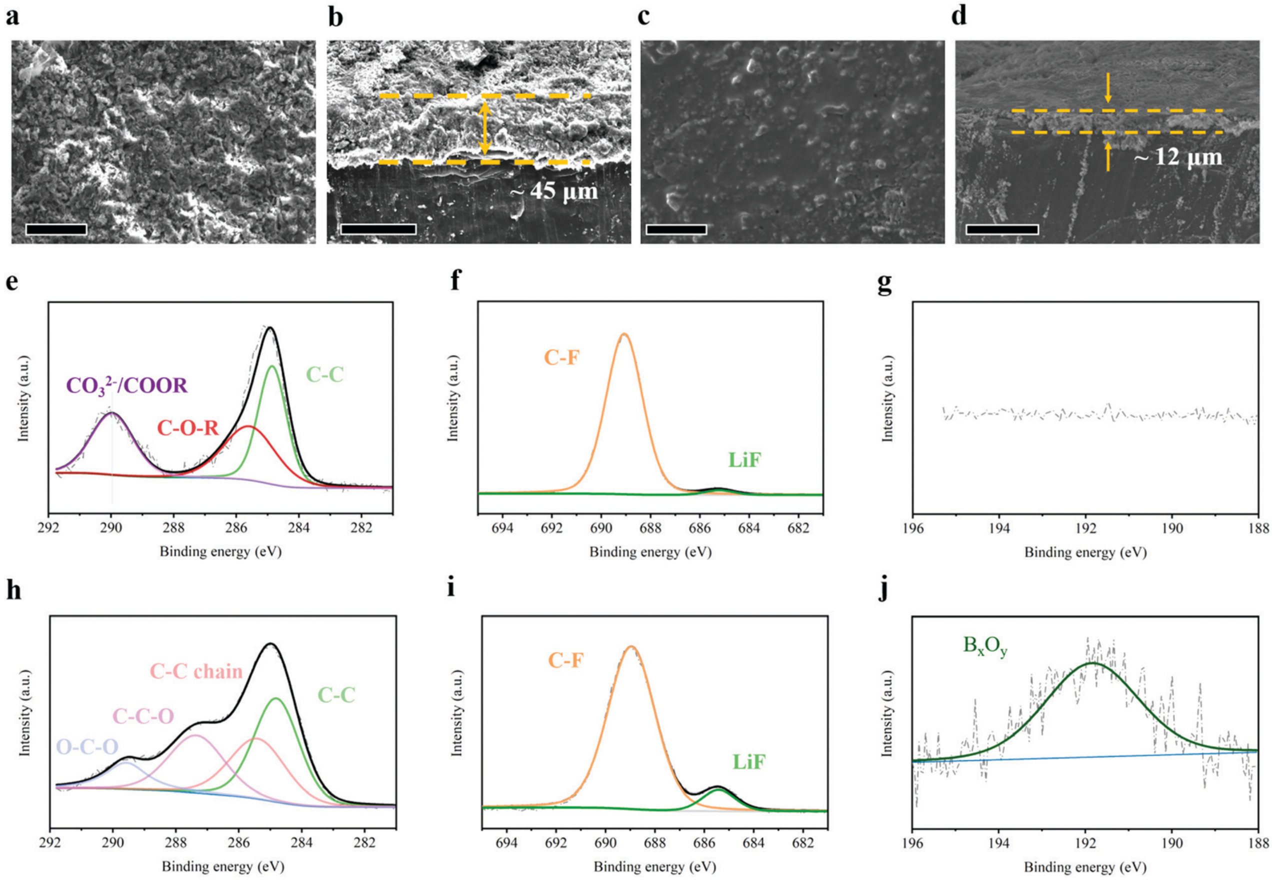

Fig. 4 Morphology surface chemistry analysis of the Li metal anodes after cycling. (a and b) Top-view (a) and cross-section (b) SEM images of Li metal after 50 cycles in LDE. (c and d) Top-view (c) and cross-section (d) SEM images of Li metal after 50 cycles in PDE. (e–j) Corresponding XPS spectra of C 1s (e and h), F 1s (f and i), B 1s (g and j) for Li metal cycled in LDE (e–g) and PDE (h–j). Scale bars, 20 μm (a and c), scale bars, 50 μm (b and d).

Due to the reduction of TB on anode surface, a much higher concentration of LiF is detected, implying a LiF-rich SEI film formed which plays a vital role in the improvement of the electrode/electrolyte interface stability.[51,52] Simultaneously, the signal of B element derived from the decomposition product of TB is also detected (Fig. 4j). The B_xO_y generated from the TB decomposition is involved in the construction of SEI, while the O–B–O bonding contributes to the formation of a cross-linked covalent skeleton, which is beneficial for the formation of stable and robust SEI, thus enhancing the stability of Li metal anode.[53]

The CE was evaluated by the asymmetric Li|Cu cells, as shown in Fig. 5a. The initial CE of the LDE cell is only 47.2% at 0.5 mA cm^{-2} for 0.5 mA h cm^{-2} and it fluctuates dramatically after 100 cycles. Meanwhile, the plating/stripping overpotential of LDE increases sharply with cycles (Fig. 5b). The rapid deterioration of CE and increasing overpotential are attributed to the instability of the SEI in the LDE system, which cannot effectively passivate the lithium anode so that the side reactions between Li metal and electrolyte continues. In striking contrast, the cell with PDE electrolyte achieves an initial CE of 86.2% and stabilized at 98.1% over 200 cycles, demonstrating a much higher and more stable CE. What is more, the plating/stripping voltage profiles remain stable throughout, indicative of a stable interface structure with low impedance. In addition, the deposition and dissolution behaviour of Li ions were further investigated. Fig. S8 (ESI†) shows the cross-section SEM images of Li-Cu batteries with LDE (a) and PDE (b) after 100 cycles at 0.5 mA cm^{-2} for 0.5 mA h cm^{-2}. It can be clearly seen that the surface of the Cu foil for LDE is covered with a significant number of Li dendrites and the thickness of the loose and porous deposited Li reaches up to ~25 μm. In contrast to LDE, the surface of the deposited Li for PDE is relatively smooth and no Li dendrite can be found. The thickness of the dense deposited Li for PDE is only ~8 μm, indicating a uniform and dense deposition of Li ions. The symmetric Li|Li cells were further assembled to evaluate the electrochemical stability of the electrolyte against Li metal. As shown in Fig. 5c, a significant increase in polarization is observed in LDE after 120 h cycles at 0.5 mA cm^{-2} for 0.5 mA h cm^{-2}. While the PDE system exhibits a consistent performance without obvious polarization increasing after even 2000 h cycles (Fig. 5d). When the current density increases to 1 mA cm^{-2}, the overpotential stabilizes at 18 mV for 800 h (Fig. 5e and f).

Full cell demonstration of PDE

The Li–S system has drawn worldwide attention in recent years for its high theoretical energy density. However, the well-known

Published on 29 2021. Downloaded by Fail Open on 23.07.2025 09:12:30.

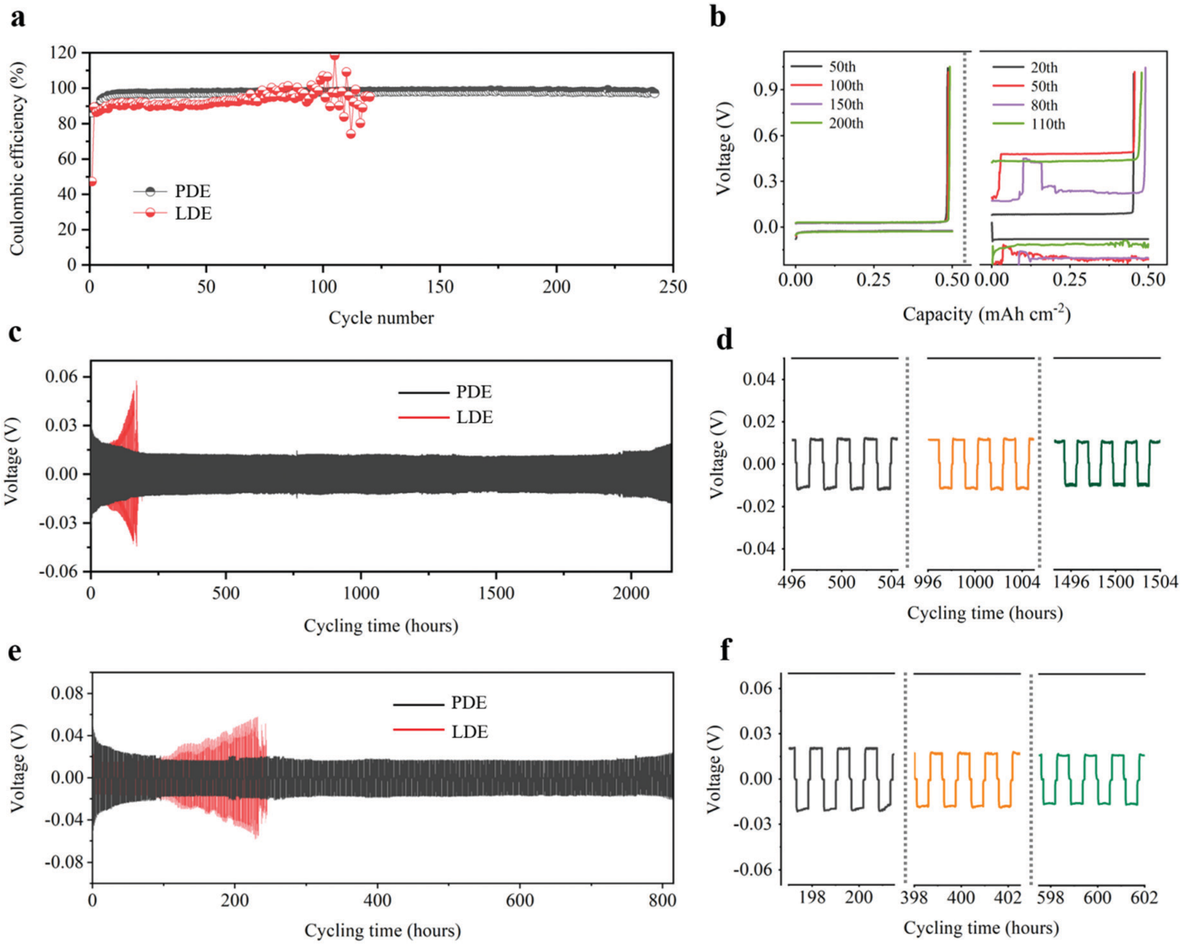

Fig. 5 Electrochemical tests of Li|Cu and Li|Li batteries with LDE and PDE. (a and b) CE (a) and corresponding voltage profiles (b) of Li|Cu batteries with LDE and PDE. (c–f) Galvanostatic cycling (c and e) and corresponding voltage profiles (d and f) of Li|Li symmetric batteries with LDE and PDE at 0.5 mA cm^{-2} (c) and 1 mA cm^{-2} (e) for 0.5 mA h cm^{-2}.

"shuttle effects" in Li–S batteries causes rapid capacity fading and poor CE, which seriously plagues its market penetration. As shown in Fig. 6a, the Li–S battery with LDE exhibits a rapid capacity fading at room temperature from 1054 to 432 mA h g^{-1} after 100 cycles at 0.2C and only maintains 240 mA h g^{-1} after 550 cycles. Without LiNO$_3$ as electrolyte additive, the CE is less than 80% during the first 50 cycles and only maintains ~90% after 550 cycles, indicative of an ever-present shuttle effect. The S cathode after long cycles with LDE shows a heavily damaged morphology with large cracks on the surface (Fig. S9a and b, ESI†) and the yellow separator indicates a large amount of LiPSs have dissolved into the electrolyte. The surface of the Li metal anode is covered by Li dendrites after cycles (Fig. S9c, ESI†). What is worse, the liquid electrolyte is almost completely consumed by the side reactions between the electrode and the electrolyte during cycles, which greatly deteriorates the ion transport between the electrodes (Fig. S9b, ESI,† inset). As to the Li–S battery using PDE, it obtains an initial capacity of 1060 mA h g^{-1} at 0.2C and maintains 660 mA h g^{-1} throughout 550 cycles, showing an ultraslow capacity decay rate of 0.094%. And the CE remains ~97% throughout 550 cycles, demonstrating an excellent long cycle stability. When the current rate increases to 0.4C (670 mA g^{-1}), the polymer battery can still exhibit stable cycling performance, which remains 600 mA h g^{-1} after 200 cycles with a CE of ~99% (Fig. 6b). Even when the current density increases to 1C, it still delivers 533 mA h g^{-1} after 120 cycles. By comparing the rate performances of the battery with LDE, it further demonstrates that the battery with PDE has better rate performances. In addition, the solid Li–S battery based on PDE with high S loading (4 mg cm^{-2}) also shows good cycling performance and the capacity decay rate is only 0.23% per cycle (Fig. S10, ESI†). Subsequently, the Li–S batteries before and after cycles were disassembled to further investigate the reason for the improved electrochemical performances. The S cathode in the fresh polymer battery is homogeneously covered by PDE (Fig. S9d, ESI†); after 100 cycles, the fully charged S cathode still remains an intact structure (Fig. S9e, ESI†). The separator is filled with polymer electrolyte throughout (Fig. S9e, ESI,† inset), which guarantees the ion transport during long-term cycles; furthermore, no obvious yellow areas are observed on the separator, implying that the dissolution and diffusion of LiPSs have been suppressed successfully. In addition, the SEM image

This journal is © The Royal Society of Chemistry 2021

Published on 29 2021. Downloaded by Fail Open on 23.07.2025 09:12:30.

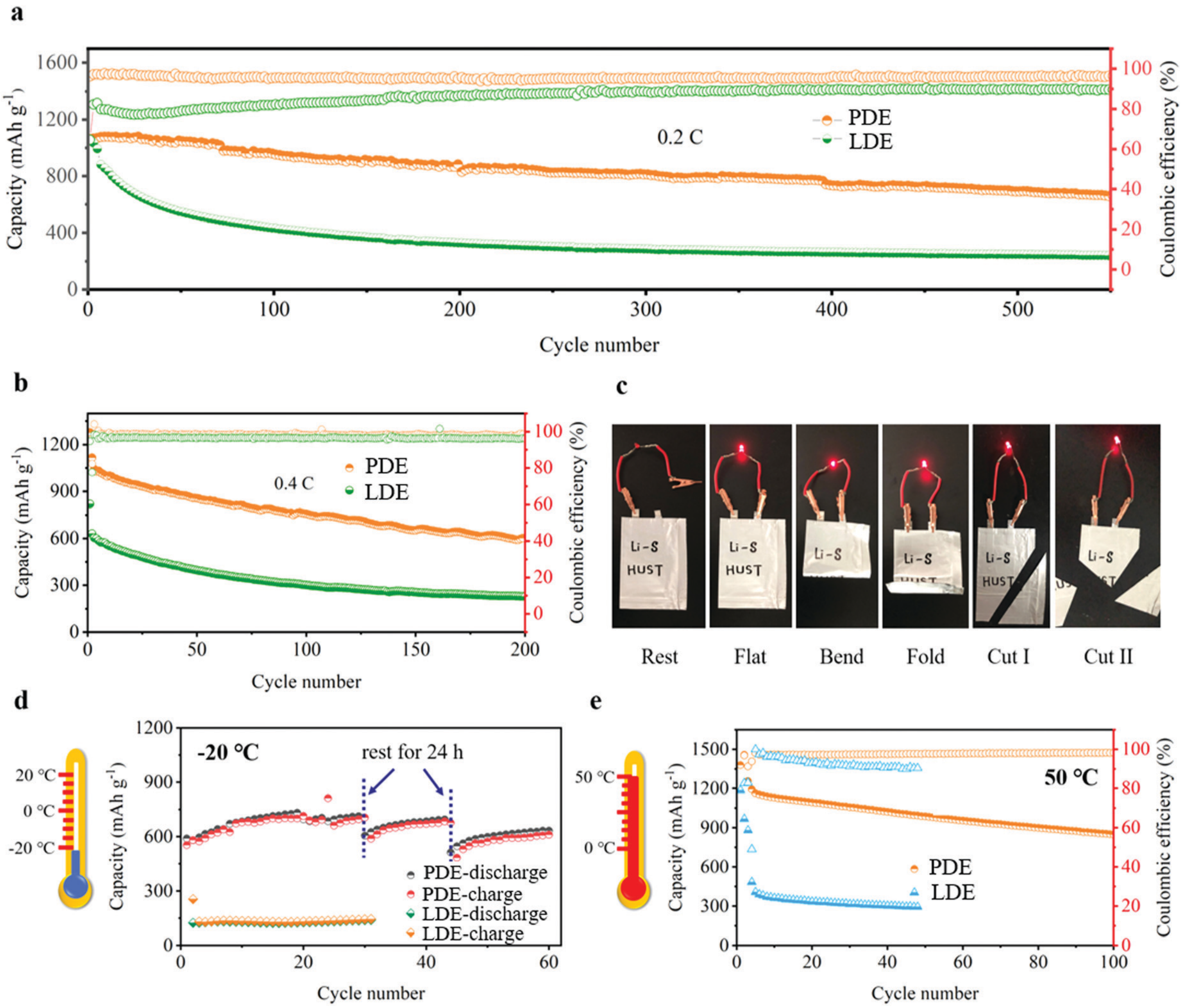

Fig. 6 Electrochemical performances of Li–S batteries. (a and b) Cycling performances and CE of Li–S batteries at room temperature with LDE and PDE at 0.2C (a) and 0.4C (b). (c) A Li–S punch cell lighting a LED lamp after being bent, folded and cut. (d and e) Cycling performances of Li–S batteries at −20 °C (d) and 50 °C (e) with LDE and PDE.

of the Li metal anode after cycles shows that the Li dendrite growth has also been effectively suppressed (Fig. S9f, ESI†).

A Li–S pouch cell with PDE was further prepared to investigate the flexibility of the polymer battery under various mechanical abuses. As shown in Fig. 6c, the pouch cell can work well after being bent and folded. Even after being cut into pieces, the pouch cell can still be able to power the LED lamp. It is attributed to the fact that PDE is much more stable than LDE, which is not easy to leak or volatilize, so after the pouch cell was cut, PDE can still maintain the reaction interface of the cathode/electrolyte/anode to ensure the normal operation of the cell. What is more, benefiting from the *in situ* polymerization method, the liquid electrolyte precursor is fully filled into the pores of the electrodes before the solidification, resulting in a tight bond between the electrolyte and the electrodes. This PDE-wrapped electrode can avoid being directly exposed to the air even after the cell is cut, thus preventing the side reactions between electrodes and the air and guaranteeing the regular operation of the cell. Obviously, PDE has excellent thermal stability and the battery with PDE has conformal and stable electrode/electrolyte interface. All these contribute to the greatly improved resistance of the polymer battery to mechanical abuse. The polymer battery can also work in a wide temperature range. Fig. 6d and e show the cycle performances of Li–S batteries with different electrolytes at −20 °C and 50 °C. The battery using LDE cannot work at all at −20 °C due to the tendency of LiPSs to aggregate at low-temperature conditions;[54] when the temperature rises to 50 °C (Fig. 6e), a rapid capacity fade of the battery is observed because of the faster diffusion of LiPSs and the gasification of the solvent. Compared with LDE, PDE as a polymer electrolyte has better thermal stability and can suppress the dissolution of LiPSs more effectively, thus improving the performance of batteries at low and high temperature. Therefore, the battery using PDE remains a high reversible capacity of ∼700 mA h g^{-1} at −20 °C and the capacity can recover even after resting for 24 h; it also demonstrates stable cycling at 50 °C, which maintains a reversible capacity of 848 mA h g^{-1} after 100 cycles at 0.5C.

Published on 29 2021. Downloaded by Fail Open on 23.07.2025 09:12:30.

The linear sweep voltammetry (LSV) measurements verify the oxidative stability of PDE has increased from 4.0 V of DOL to 4.8 V *versus* Li/Li$^+$ (Fig. 7a), which makes it suitable to match the electrolyte with high-voltage cathodes. The poor resistance to high voltage oxidation of DOL is mainly attributed to its unstable cyclic structure. After the ring-opening polymerization, the structural stability of long-chain linear of DOL is greatly improved, and thus the resistance to high-voltage oxidation is significantly enhanced. The Li|PDE|NCM$_{622}$ battery operate in the voltage range of 3.0 to 4.3 V. As shown in Fig. 7b, the Li|LDE|NCM$_{622}$ battery delivers an initial reversible capacity of only 104 mA h g^{-1} and fails after only 4 cycles. The voltage polarization during the charge/discharge cycles keeps increasing constantly until the battery fails totally (Fig. S11, ESI†). In stark contrast, the Li|PDE|NCM$_{622}$ battery can maintain a reversible capacity of 132 mA h g^{-1} after 200 cycles at 0.5C and the polarization keeps relatively stable during cycles (Fig. 7c). In addition, LiFePO$_4$, another widely applied cathode material, also shows excellent compatibility with PDE. Fig. 7d and e show the long-term cycling performance and corresponding voltages profiles of the Li|LiFePO$_4$ battery using PDE. It maintains a reversible capacity of 122 mA h g^{-1} with almost no capacity degradation or polarization change over 1200 cycles at 2C rate. It is well known that the toughest problem in the LMB is the side reactions between the electrolyte and the highly active lithium, which generally features as the low CE and the exhaustion of the electrolyte. Since the side reactions of Li always generate gas products, the gas products can be used as a sign signal for the side reactions. Based on this understanding, ultrasonic transmission mappings, which is an effective non-destructive technique developed by our group to investigate the state of the electrolyte inside a pouch cell,[55,56] were performed to test Li|LiFePO$_4$ pouch cells to study the side reactions during cycles. As shown in Fig. S12 (ESI†), ultrasound waves are emitted from a focused transducer on one side and penetrate the cell, where they are subsequently received by a transducer on the other side. Changes in the physical properties of the material can affect the transmission of the ultrasound signal. Because the acoustic impedance of gases differs greatly from that of solids and liquids, the ultrasonic transmissivity at the gas–liquid and gas-solid interfaces will be sharply attenuated. Therefore, even if only a small amount of gas is generated, it can be detected by ultrasonic transmission mappings. The ultrasonic transmission mapping images were

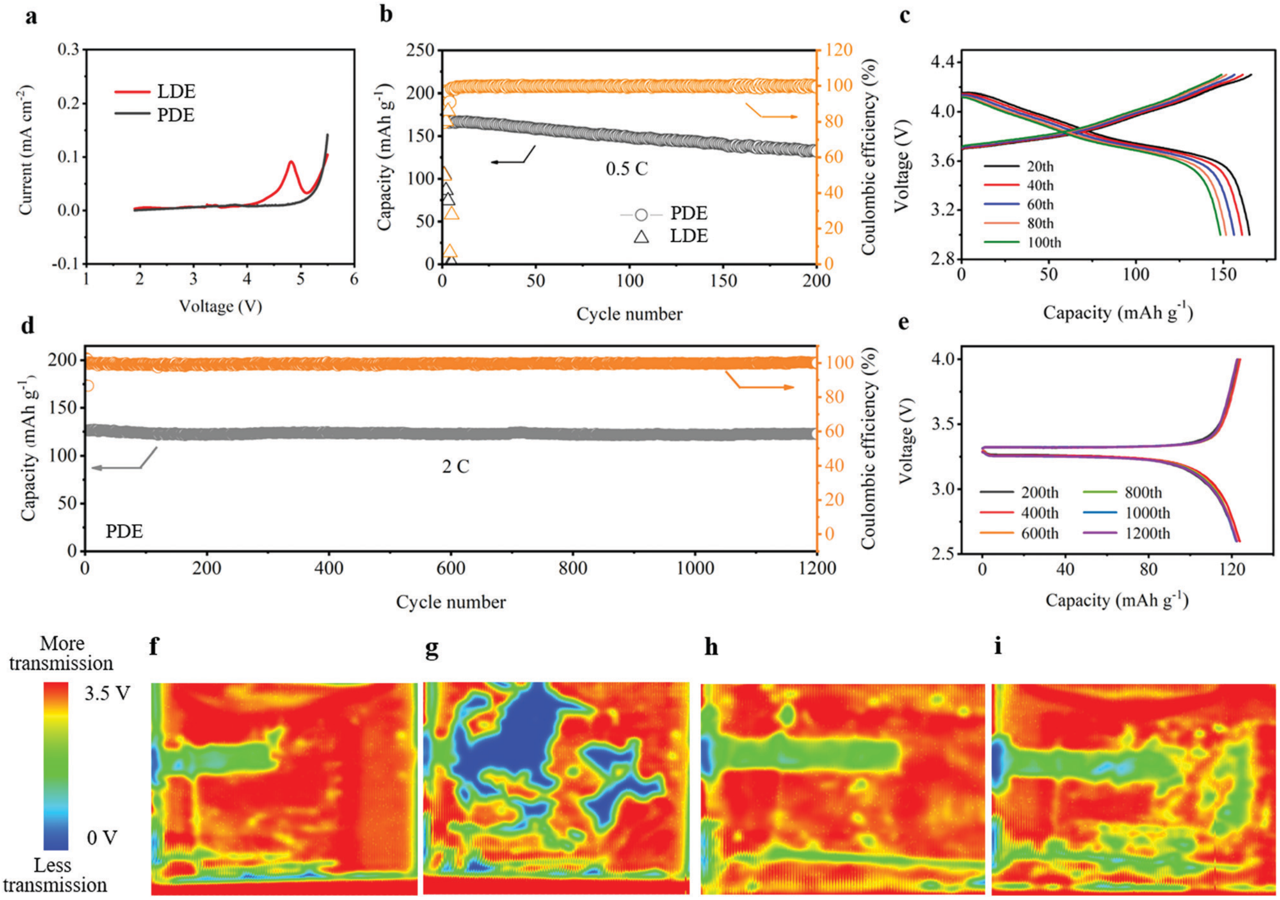

Fig. 7 Electrochemical performances of full cells with NCM$_{622}$ and LiFePO$_4$ as the cathodes. (a) LSV curves of LDE and PDE with a range of voltages from 1.9 to 5.5 V at room temperature. (b) Cycling performance and CE of Li|NCM$_{622}$ using PDE and LDE at 0.5C. (c) Corresponding voltages profiles of Li|NCM$_{622}$ using PDE from 20th to 100th. (d and e) Cycling performance, CE (d) and corresponding voltage profiles (e) of Li|LiFePO$_4$ using PDE. (f–i) Ultrasonic transmission mappings of the Li|LiFePO$_4$ using LDE (f and g) and PDE (h and i) before (f and h) and after 30 cycles (g and i).

This journal is © The Royal Society of Chemistry 2021

Published on 29 2021. Downloaded by Fail Open on 23.07.2025 09:12:30.

obtained from an ultrasonic battery scanner (Fig. S13, ESI,† more details of the experiment are as described in the Methods). According to the given scale bar (between 0 and 3.5 V), the red and blue correspond to the high and low transmission regions, respectively. The gas generated inside a cell will result in the attenuation of the ultrasonic transmissivity. Fig. 7f and h display the ultrasonic transmission mapping images of the Li|$LiFePO_4$ pouch cells using LDE and PDE before cycles, respectively. The equally distributed red areas indicate good electrode wetting within the entire cells (the green areas correspond to the taps and the residual gas near the seal, which reduce the transmission of the ultrasonic wave). After 30 cycles, large blue areas appeared on the transmission mapping image of Li|LDE|$LiFePO_4$ pouch cell indicates the un-wetting process within the battery (Fig. 7g), implying the decomposition of the electrolyte. In contrast, the Li|PDE|$LiFePO_4$ pouch cell keeps relatively high ultrasonic transmissivity throughout the cycles (Fig. 7i), demonstrating the stability of PDE during cycles.

Conclusions

In summary, a novel *in situ* formed poly-DOL electrolyte with high ionic conductivity, good flame retardancy, significantly expanded operating temperature limit and oxidative stability window, is well designed by adding a low concentration of TB as a multifunctional additive. The poly-DOL electrolyte greatly improves the performance of LMBs in five aspects. (1) Good interfacial wettability. Benefited from the good wettability of the low viscous precursor solvent, an integrated three-dimensional network throughout the whole battery forms after the *in situ* polymerization, which guarantees the compact contact between the electrolyte and the electro-active particles. (2) Outstanding compatibility with Li metal anode. The TB with high fluoride content contributes to the formation of a stable LiF-rich SEI, thus suppressing the growth of Li dendrites and improving the stability of Li metal anode during long-term cycles. (3) Excellent thermal stability. The decomposition of TB generates fluorine free radicals which can effectively trap the highly reactive radicals, thus making PDE non-flammable and therefore enhancing the safety of LMBs. (4) A wide temperature range for application. Benefiting from the interaction between TB and $TFSI^-$ anion, the Li-ion transference number of PDE is significantly increased, which improves the transmission capability of Li-ion in the electrolyte and facilitates the operation of the battery at low temperature. (5) A significant expanded electrochemical stability region. The oxidative stability of PDE has increased from 4.0 V to 4.8 V because of the stable long chain linear structure of DOL, which makes it suitable to match with high-voltage cathodes. Benefitting from these advantages of PDE, applications of the PDE in Li–S, Li–NCM_{622} and Li–$LiFeO_4$ batteries all demonstrate excellent electrochemical performances. The Li–S batteries deliver an initial capacity of 1060 mA h g^{-1} at 0.2C and shows an ultraslow capacity decay rate of 0.094% throughout 550 cycles. When the temperature varies from −20 to 50 °C, it still provides a stable cycling performance. The high voltage Li–$LiNi_{0.6}Co_{0.2}Mn_{0.2}O_2$ and Li–$LiFePO_4$ batteries both exhibit excellent capacity output and long-term cycle stability (>1200 cycles). Moreover, ultrasonic transmission mappings, which is an effective non-destructive technique developed by our group to investigate the state of the electrolyte inside a pouch cell, show no gas generation in the Li|PDE|LiFePO4 pouch cell during cycles, further demonstrating the stability of PDE. This study provides new insights into the design of the advanced electrolyte system for high-energy-density LMBs.

Author contributions

J. W. X. and Y. Z. had equal contribution to the article. J. W. X. designed the experiments and wrote the article; J. W. X. and Y. Z. carried out the materials synthesis and the electrochemical evaluation. B. Z. performed the Molecular dynamics simulations and the related analysis. L. X. Y. raised the idea, analyzed the data and edited the manuscript. X. T. L. helped perform ultrasonic measurements on cells. Z. X. C., Y. Y. and X. X. Z. helped characterize the samples. Z. L. and Y. S. offered valuable advices and helped edit the manuscript. Y. H. H. raised the idea, gave helpful discussions and revised the manuscript. All authors have read and approved the final manuscript.

Conflicts of interest

There are no conflicts to declare.

Acknowledgements

This work was supported by the National Science Foundation of China (Grant No. 22075091, 21773077, 51632001, and 51532005), Postdoctoral Innovation Talent Support Program of China (Grant No. BX20200139) and the National Key R&D Program of China (2018YFB0905400). The authors acknowledge the Analytical and Testing Center of Huazhong University of Science and Technology (HUST) for XPS, field emission TEM and the State Key Laboratory of Materials Processing and Die and Mould Technology of HUST for SEM.

Notes and references

1 M. Winter, B. Barnett and K. Xu, *Chem. Rev.*, 2018, **118**, 11433–11456.
2 J. Xiang, L. Yang, L. Yuan, K. Yuan, Y. Zhang, Y. Huang, J. Lin, F. Pan and Y. Huang, *Joule*, 2019, **3**, 2334–2363.
3 J. B. Goodenough and K. S. Park, *J. Am. Chem. Soc.*, 2013, **135**, 1167–1176.
4 P. G. Bruce, S. A. Freunberger, L. J. Hardwick and J. M. Tarascon, *Nat. Mater.*, 2011, **11**, 19–29.
5 W. Xu, J. Wang, F. Ding, X. Chen, E. Nasybulin, Y. Zhang and J.-G. Zhang, *Energy Environ. Sci.*, 2014, **7**, 513–537.
6 D. Lin, Y. Liu and Y. Cui, *Nat. Nanotechnol.*, 2017, **12**, 194–206.

This journal is © The Royal Society of Chemistry 2021

Published on 29 2021. Downloaded by Fail Open on 23.07.2025 09:12:30.

7 X. B. Cheng, R. Zhang, C. Z. Zhao and Q. Zhang, *Chem. Rev.*, 2017, **117**, 10403–10473.
8 J. Xiang, L. Yuan, Y. Shen, Z. Cheng, K. Yuan, Z. Guo, Y. Zhang, X. Chen and Y. Huang, *Adv. Energy Mater.*, 2018, **8**, 1802352.
9 Z. Lin, T. Liu, X. Ai and C. Liang, *Nat. Commun.*, 2018, **9**, 5262.
10 S. H. Wang, J. Yue, W. Dong, T. T. Zuo, J. Y. Li, X. Liu, X. D. Zhang, L. Liu, J. L. Shi, Y. X. Yin and Y. G. Guo, *Nat. Commun.*, 2019, **10**, 4930.
11 J. Wu, L. Yuan, W. Zhang, Z. Li, X. Xie and Y. Huang, *Energy Environ. Sci.*, 2021, **14**(1), 12–36, DOI: 10.1039/d0ee02241a.
12 K. Fu, Y. Gong, G. T. Hitz, D. W. McOwen, Y. Li, S. Xu, Y. Wen, L. Zhang, C. Wang, G. Pastel, J. Dai, B. Liu, H. Xie, Y. Yao, E. D. Wachsman and L. Hu, *Energy Environ. Sci.*, 2017, **10**, 1568–1575.
13 C. Wang, L. Zhang, H. Xie, G. Pastel, J. Dai, Y. Gong, B. Liu, E. D. Wachsman and L. Hu, *Nano Energy*, 2018, **50**, 393–400.
14 X.-B. Cheng, C.-Z. Zhao, Y.-X. Yao, H. Liu and Q. Zhang, *Chem*, 2019, **5**, 74–96.
15 J. Liang, J. Luo, Q. Sun, X. Yang, R. Li and X. Sun, *Energy Storage Mater.*, 2019, **21**, 308–334.
16 Q. Zhao, S. Stalin, C.-Z. Zhao and L. A. Archer, *Nat. Rev. Mater.*, 2020, **5**, 229–252.
17 Q. Zhou, J. Ma, S. M. Dong, X. F. Li and G. L. Cui, *Adv. Mater.*, 2019, **31**, 1902029.
18 T. Dong, J. Zhang, G. Xu, J. Chai, H. Du, L. Wang, H. Wen, X. Zang, A. Du, Q. Jia, X. Zhou and G. Cui, *Energy Environ. Sci.*, 2018, **11**, 1197–1203.
19 J. Dai, K. Fu, Y. Gong, J. Song, C. Chen, Y. Yao, G. Pastel, L. Zhang, E. Wachsman and L. Hu, *ACS Mater. Lett.*, 2019, **1**, 354–361.
20 S. Li, S. Q. Zhang, L. Shen, Q. Liu, J. B. Ma, W. Lv, Y. B. He and Q. H. Yang, *Adv. Sci.*, 2020, **7**, 1903088.
21 H. Li, C. Han, Y. Huang, Y. Huang, M. Zhu, Z. Pei, Q. Xue, Z. Wang, Z. Liu, Z. Tang, Y. Wang, F. Kang, B. Li and C. Zhi, *Energy Environ. Sci.*, 2018, **11**, 941–951.
22 D. Lin, P. Y. Yuen, Y. Liu, W. Liu, N. Liu, R. H. Dauskardt and Y. Cui, *Adv. Mater.*, 2018, **30**, e1802661.
23 J. Wu, Z. Rao, Z. Cheng, L. Yuan, Z. Li and Y. Huang, *Adv. Energy Mater.*, 2019, **9**, 1902767.
24 G. Chen, F. Zhang, Z. Zhou, J. Li and Y. Tang, *Adv. Energy Mater.*, 2018, **8**, 1801219.
25 Z. Lin, X. Guo and H. Yu, *Nano Energy*, 2017, **41**, 646–653.
26 S. Z. Zhang, X. H. Xia, D. Xie, R. C. Xu, Y. J. Xu, Y. Xia, J. B. Wu, Z. J. Yao, X. L. Wang and J. P. Tu, *J. Power Sources*, 2019, **409**, 31–37.
27 L. Chen, Y. Li, S.-P. Li, L.-Z. Fan, C.-W. Nan and J. B. Goodenough, *Nano Energy*, 2018, **46**, 176–184.
28 W. Liu, S. W. Lee, D. Lin, F. Shi, S. Wang, A. D. Sendek and Y. Cui, *Nat. Energy*, 2017, **2**, 1–7.
29 O. Sheng, C. Jin, J. Luo, H. Yuan, H. Huang, Y. Gan, J. Zhang, Y. Xia, C. Liang, W. Zhang and X. Tao, *Nano Lett.*, 2018, **18**, 3104–3112.
30 Y. Hu, Y. Zhong, L. Qi and H. Wang, *Nano Res.*, 2020, **13**, 3230–3234.
31 D. Zhou, D. Shanmukaraj, A. Tkacheva, M. Armand and G. Wang, *Chem*, 2019, **5**, 2326–2352.
32 Y. G. Cho, C. Hwang, D. S. Cheong, Y. S. Kim and H. K. Song, *Adv. Mater.*, 2019, **31**, e1804909.
33 Q. Zhou, S. M. Dong, Z. L. Lv, G. J. Xu, L. Huang, Q. L. Wang, Z. L. Cui and G. L. Cui, *Adv. Energy Mater.*, 2020, **10**, 1903441.
34 S. Liang, W. Yan, X. Wu, Y. Zhang, Y. Zhu, H. Wang and Y. Wu, *Solid State Ionics*, 2018, **318**, 2–18.
35 D. Zhou, Y.-B. He, Q. Cai, X. Qin, B. Li, H. Du, Q.-H. Yang and F. Kang, *J. Mater. Chem. A*, 2014, **2**, 20059–20066.
36 M. Liu, D. Zhou, Y.-B. He, Y. Fu, X. Qin, C. Miao, H. Du, B. Li, Q.-H. Yang, Z. Lin, T. S. Zhao and F. Kang, *Nano Energy*, 2016, **22**, 278–289.
37 Y. Ma, J. Ma, J. Chai, Z. Liu, G. Ding, G. Xu, H. Liu, B. Chen, X. Zhou, G. Cui and L. Chen, *ACS Appl. Mater. Interfaces*, 2017, **9**, 41462–41472.
38 Q. Zhao, X. Liu, S. Stalin, K. Khan and L. A. Archer, *Nat. Energy*, 2019, **4**, 365–373.
39 F. Q. Liu, W. P. Wang, Y. X. Yin, S. F. Zhang, J. L. Shi, L. Wang, X. D. Zhang, Y. Zheng, J. J. Zhou, L. Li and Y. G. Guo, *Sci. Adv.*, 2018, **4**, eaat5383.
40 J. Liu, X. Shen, J. Zhou, M. Wang, C. Niu, T. Qian and C. Yan, *ACS Appl. Mater. Interfaces*, 2019, **11**, 45048–45056.
41 H. Wu, B. Tang, X. F. Du, J. J. Zhang, X. R. Yu, Y. T. Wang, J. Ma, Q. Zhou, J. W. Zhao, S. M. Dong, G. J. Xu, J. N. Zhang, H. Xu, G. L. Cui and L. Q. Chen, *Adv. Sci.*, 2020, **7**, 2003370.
42 S. Huang, Z. Cui, L. Qiao, G. Xu, J. Zhang, K. Tang, X. Liu, Q. Wang, X. Zhou, B. Zhang and G. Cui, *Electrochim. Acta*, 2019, **299**, 820–827.
43 Y. Cui, X. Liang, J. Chai, Z. Cui, Q. Wang, W. He, X. Liu, Z. Liu, G. Cui and J. Feng, *Adv. Sci.*, 2017, **4**, 1700174.
44 H. Chen, D. Adekoya, L. Hencz, J. Ma, S. Chen, C. Yan, H. Zhao, G. Cui and S. Zhang, *Adv. Energy Mater.*, 2020, **10**, 2000049.
45 S. Ramesh and H. M. Ng, *Solid State Ionics*, 2011, **192**, 2–5.
46 Y. Lin, X. Wang, J. Liu and J. D. Miller, *Nano Energy*, 2017, **31**, 478–485.
47 J. C. Lassegues, J. Grondin and D. Talaga, *Phys. Chem. Chem. Phys.*, 2006, **8**, 5629–5632.
48 D. M. Seo, O. Borodin, S.-D. Han, P. D. Boyle and W. A. Henderson, *J. Electrochem. Soc.*, 2012, **159**, A1489–A1500.
49 R. Rojaee, S. Cavallo, S. Mogurampelly, B. K. Wheatle, V. Yurkiv, R. Deivanayagam, T. Foroozan, M. G. Rasul, S. Sharifi-Asl, A. H. Phakatkar, M. Cheng, S. B. Son, Y. Pan, F. Mashayek, V. Ganesan and R. Shahbazian-Yassar, *Adv. Funct. Mater.*, 2020, **30**, 1910749.
50 Y. Wang, C. F. Lin, J. Rao, K. Gaskell, G. Rubloff and S. B. Lee, *ACS Appl. Mater. Interfaces*, 2018, **10**, 24554–24563.
51 W. Xue, Z. Shi, M. Huang, S. Feng, C. Wang, F. Wang, J. Lopez, B. Qiao, G. Xu, W. Zhang, Y. Dong, R. Gao, Y. Shao-Horn, J. A. Johnson and J. Li, *Energy Environ. Sci.*, 2020, **13**, 212–220.
52 J. Chen, X. Fan, Q. Li, H. Yang, M. R. Khoshi, Y. Xu, S. Hwang, L. Chen, X. Ji, C. Yang, H. He, C. Wang,

This journal is © The Royal Society of Chemistry 2021

Published on 29 2021. Downloaded by Fail Open on 23.07.2025 09:12:30.

E. Garfunkel, D. Su, O. Borodin and C. Wang, *Nat. Energy*, 2020, **5**, 386–397.

53 S. Li, W. Zhang, Q. Wu, L. Fan, X. Wang, X. Wang, Z. Shen, Y. He and Y. Lu, *Angew. Chem., Int. Ed.*, 2020, **59**(35), 14935–14941, DOI: 10.1002/anie.202004853.

54 A. Gupta, A. Bhargav, J.-P. Jones, R. V. Bugga and A. Manthiram, *Chem. Mater.*, 2020, **32**, 2070–2077.

55 Z. Deng, Z. Huang, Y. Shen, Y. Huang, H. Ding, A. Luscombe, M. Johnson, J. E. Harlow, R. Gauthier and J. R. Dahn, *Joule*, 2020, **4**, 2017–2029.

56 A. J. Louli, A. Eldesoky, R. Weber, M. Genovese, M. Coon, J. deGooyer, Z. Deng, R. T. White, J. Lee, T. Rodgers, R. Petibon, S. Hy, S. J. H. Cheng and J. R. Dahn, *Nat. Energy*, 2020, **5**, 693–702.